PHOTONICS Research

Large-signal SPICE model for depletion-type silicon ring modulators

Minkyu Kim,[1] Myungjin Shin,[1,2] Min-Hyeong Kim,[1,3] Byung-Min Yu,[1] Younghyun Kim,[1,4] Yoojin Ban,[1,4] Stefan Lischke,[5] Christian Mai,[5] Lars Zimmermann,[5] and Woo-Young Choi[1,*]

[1]Department of Electrical and Electronic Engineering, Yonsei University, 03722 Seoul, South Korea
[2]Now at University of Michigan, Ann Arbor, 48109 Michigan, USA
[3]Now at Samsung Electronics, Hwasung, 18448 Gyeonggi-do, South Korea
[4]Now at IMEC, Kapeldreef 75, 3001 Leuven, Belgium
[5]IHP, Im Technologiepark 25, 15236 Frankfurt (Oder), Germany
*Corresponding author: wchoi@yonsei.ac.kr

We present an accurate, easy-to-use large-signal SPICE circuit model for depletion-type silicon ring modulators (Si RMs). Our model includes both the electrical and optical characteristics of the Si RM and consists of circuit elements whose values change depending on modulation voltages. The accuracy of our model is confirmed by comparing the SPICE simulation results of 25 Gb/s non-return-to-zero (NRZ) modulation with the measurement. The model is used for performance optimization of monolithically integrated Si photonic NRZ and pulse-amplitude-modulation 4 transmitters in the standard SPICE circuit design environment.   © 2019 Chinese Laser Press

https://doi.org/10.1364/PRJ.7.000948

1. INTRODUCTION

Depletion-type silicon ring modulators (Si RMs) attract a great amount of research interests since they can provide advantages for optical interconnect (IC) applications such as large modulation bandwidth and small power consumption [1–4]. Furthermore, Si RMs are much smaller than the widely used Si Mach–Zehnder modulators (MZMs) and, consequently, allow much easier monolithic integration with electronics. Such electronic–photonic integration is necessary for interconnection solutions for future high-performance electronic systems in which photonic solutions must be as closely located to electronics as possible for size and power consumption reduction [5]. To realize Si electronic–photonic ICs containing Si RMs, a Si RM equivalent circuit model that is accurate, easy-to-use, and compatible with the standard IC design environment is highly desirable. In addition, extracting numerical values for model parameters should be simple and straight-forward.

Although there have been several published reports on depletion-type Si RM models, none satisfies the above requirements. In Ref. [6], a precise analytical model for a Si RM was reported, but it requires more than 10 parameters and is not very compatible with the standard Si IC design environment. We reported a Verilog-A implementation of a coupled-mode description of the Si RM [7], which can be easily executed in the SPICE simulation environment. It, however, requires a substantial amount of computation time because Verilog-A is not optimized for numerically solving differential equations

and, consequently, the simulation must use a very fine time resolution to accurately describe Si RM dynamics.

In this paper, we present a large-signal equivalent circuit model based on the linear equivalent circuit of the Si RM [8], which contains only a few independent model parameters that can be easily extracted from the simple RM transmission measurement. Although model parameter values nonlinearly depend on the Si RM bias voltage, we demonstrate that, by using voltage-dependent circuit elements available within SPICE, large-signal transient modulation characteristics can be easily and accurately simulated at least 220 times faster than the approach used in Ref. [7]. Such a reduction in computation time should provide a great advantage for design optimization of optical interconnection solutions for high-performance electronic systems that may contain numerous Si RMs as well as various electronic circuit blocks. An initial portion of this work was reported in Ref. [9]. In this paper, a more detailed description of our model is presented. In addition, we provide how our model can be used for performance optimization of pulse-amplitude modulation 4 (PAM-4) transmitters containing Si RMs and SiGe BiCMOS transistors.

This paper is organized in four chapters. In Chapter 2, after a brief description of the Si RM device used for our investigation, we give the details of our model and explain how model parameters are extracted from measurement results. The accuracy of the model also is verified with a 25 Gb/s non-return-to-zero (NRZ) measurement. In Chapter 3, we demonstrate the

advantage of our model by showing how it can be used for the design optimization of a monolithic Si photonic NRZ and PAM-4 transmitters in terms of power consumption minimization and optical modulation amplitude (OMA) maximization. Chapter 4 concludes the paper.

2. LARGE-SIGNAL SPICE MODEL FOR Si RM

Figure 1(a) shows the structure of the depletion-type Si RM used for our investigation. It is fabricated by a Si photonics foundry service provided by IHP. The ring has an 8 μm radius, and there is a 290 nm separation between the bus and ring waveguides, as can be seen in the TEM image of the cross-section of the coupling section given in Fig. 1(b). The lateral p-n junction diode for the ring waveguide has the nominal peak doping concentration of 7×10^{17} cm^{-3} for the p-region and 3×10^{18} cm^{-3} for the n-region. Figure 1(c) shows the normalized transmission characteristics measured at four different bias voltages. For this and other measurements reported in this paper, the device is placed on a stage whose temperature is maintained at 25°C by a temperature controller.

The dynamic characteristics of an RM can be described by coupled-mode equations as [10]

$$\frac{\mathrm{d}}{\mathrm{d}t}a(t) = \left(j\omega_{\mathrm{res}} - \frac{1}{\tau}\right)a(t) - j\sqrt{\frac{2}{\tau_e}}E_{\mathrm{in}}(t), \quad (1)$$

$$E_{\mathrm{out}}(t) = E_{\mathrm{in}}(t) - j\sqrt{\frac{2}{\tau_e}}a(t), \quad (2)$$

where $a(t)$ represents the energy stored in the ring resonator, and τ is the decay time constant for $a(t)$. τ has

two components, τ_l and τ_e, which, respectively, represent the decay time constants due to the ring resonator loss and the coupling loss between the ring and bus waveguides. Their relationship is given as $\frac{1}{\tau} = \frac{1}{\tau_l} + \frac{1}{\tau_e}$. ω_{res} is the ring resonance angular frequency given as $\omega_{\mathrm{res}} = \frac{2\pi mc}{n_{\mathrm{eff}}L}$, where m is an integer representing the resonance mode index, c is the velocity of light in the vacuum, L is the ring circumference, and n_{eff} is the effective index of the ring waveguide at the resonance.

The RM steady-state transmission characteristics can be derived from Eqs. (1) and (2) as

$$T = \left(\frac{E_{\mathrm{out}}}{E_{\mathrm{in}}}\right)^2 = \left[\frac{j(\omega - \omega_{\mathrm{res}}) + \frac{2}{\tau_l} - \frac{1}{\tau}}{j(\omega - \omega_{\mathrm{res}}) + \frac{1}{\tau}}\right]^2. \quad (3)$$

By fitting Eq. (3) to the measured transmission characteristics shown in Fig. 1(c), numerical values for three key parameters (n_{eff}, τ, τ_l) at different bias voltages can be determined. The results are given in Table 1. The quality factor of the RM is related to τ as $Q = \frac{\omega_{\mathrm{res}}\tau}{2}$, which indicates our RM has a Q of about 8000.

The normalized RM small-signal modulation frequency response in the s-domain at a given bias voltage can be approximated as [11]

$$\frac{s + \frac{2}{\tau_l}}{s^2 + \frac{2}{\tau}s + D_\omega^2 + \frac{1}{\tau^2}}, \quad (4)$$

where D_ω is the detuning parameter ($D_\omega = |\omega_{\mathrm{in}} - \omega_{\mathrm{res}}|$) representing how much the input light frequency (ω_{in}) is separated from the RM resonance frequency (ω_{res}). Figure 2(a) shows the block diagram of the Si RM equivalent circuit. It consists of three blocks. Block A accounts for parasitic RLC components due to bond pads and metal interconnects [8]. Block B shown
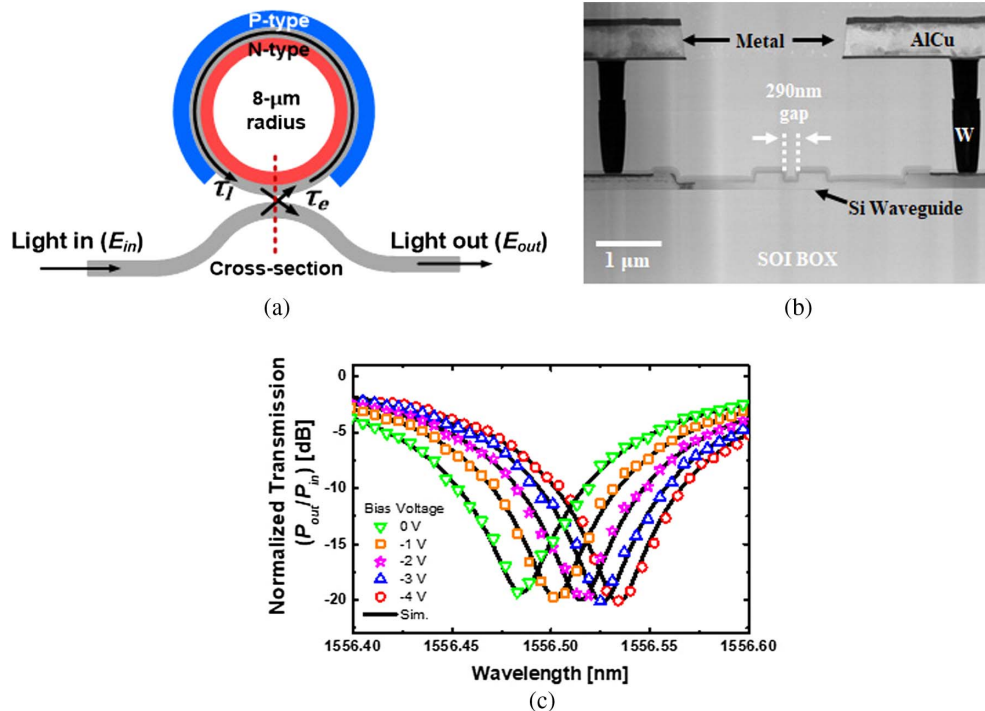
Fig. 1. (a) Structure of the Si RM used; (b) TEM image of the cross-section of the coupling section; and (c) measured transmission curves with different bias voltages.

Table 1. Extracted Si RM Parameters at Different Bias Voltages

V_{Bias} (V)	n_{eff}	τ_l (ps/rad)	τ (ps/rad)
0	2.632166	22.7239	12.8595
−1	2.632185	22.9560	12.9335
−2	2.632216	23.5576	13.1224
−3	2.632233	23.5578	13.1225
−4	2.632250	23.5579	13.1225
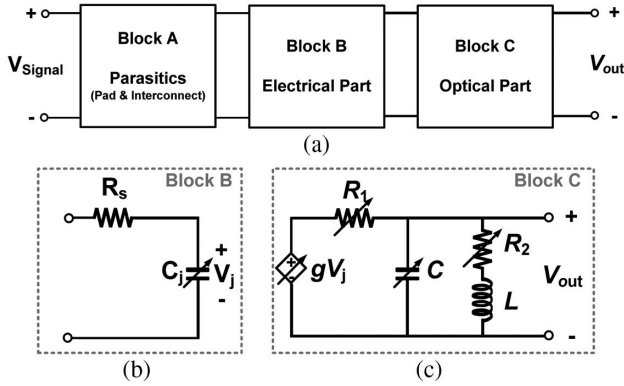
Fig. 2. (a) Three blocks for the Si RM model; (b) circuit representing RM electrical property; and (c) equivalent circuit representing RM optical property.

in Fig. 2(b) represents the RM's electrical property due to a series resistance and ring waveguide p-n junction. Block C shown in Fig. 2(c) is an equivalent circuit emulating Eq. (4). Voltage-dependent resistors and capacitors are used in Blocks B and C, as the junction capacitance, and τ and τ_l depend on RM bias voltages. A scaling factor given as $g = \frac{P_{out}}{P_{in}} \cdot \frac{R_1+R_2}{R_2}$ is used in Block C, where P_{in} and P_{out} are the input and output optical power used for the RM transmission measurement, respectively, so that Block C output voltage, V_{out}, represents the ratio of P_{out} and P_{in}.

Numerical values for circuit elements in Blocks A and B can be easily obtained from the electrical *s*-parameter measurements at different bias voltages. Numerical values for Block C circuit elements are obtained by matching Eq. (4) with the Block C transfer function given as

$$\frac{s + \frac{R_2}{L}}{s^2 + \left(\frac{1}{CR_1} + \frac{R_2}{L}\right)s + \frac{1}{LC}\left(\frac{R_2}{R_1} + 1\right)}, \tag{5}$$

using extracted numerical values for n_{eff}, τ, and τ_l at different bias voltages and detuning values. Table 2 shows the extracted numerical values for Block C circuit elements for two different cases of detuning wavelengths. The circuit models given in Block B and Block C are small signal models whose parameter values depend on bias voltages. With parameter values determined at a few sample bias voltages, large-signal behavior modeling can be easily done using the piece-wise linear simulation capability available in SPICE. Here, the detuning wavelength given as $D_\lambda = \frac{2\pi c}{D_\omega}$ is used because it is more convenient to use in measurement. As can be seen in the table, R_s is independent of the bias voltage and detuning, and C_j is independent of detuning. Since Eq. (4) has three independent variables (τ_l, τ, D_ω) and Eq. (5) has four (R_1, R_2, L, C), we arbitrarily fix the value of R_2 at a 0 bias voltage as 10,000 Ω and then determine other circuit parameter values at the same bias voltages. For other bias voltages, we fix the value of L at the value determined at 0 bias voltage and modify other resistor and capacitor values since variable resistors and capacitors are much easier to use in SPICE than the variable inductor. R_2 does not change with D_λ since τ_l does not depend on D_λ. On the other hand, R_1 is proportional to D_λ, and $R_1 C$ is proportional to τ_e, which does not depend on D_λ. Consequently, C decreases with D_λ.

The voltage-dependent circuit elements in Fig. 2(b) can be easily implemented with the piece-wise linear (PWL) elements available in SPICE. Using this approach, the large-signal RM eye diagrams can be very easily simulated in SPICE. Although parameter values at only five different biases are specified for our investigation, the simulator automatically interpolates the values at other bias voltages, providing very accurate and efficient simulation results. Figure 3 shows both the measured and simulated (red lines) 25 Gb/s Si RM eye diagrams for several detuning values. For both, modulating signals are $2^{31} - 1$ PRBS having $4V_{peak-to-peak}$ with −2 V common mode voltage. For simulation, Synopsys HSPICE, Version M 2017.03, is used. In addition, S21 responses of RF cables, the oscilloscope (Tektronix CSA8000B and 80E03), and the optical receiver (Optilab PR-23-M) [12] used in the measurement are included to achieve an accurate comparison. As can be seen, the simulation based on the RM equivalent circuit provides good agreement with the measurement results. For a 1 μs long transient simulation with a 0.1 ps time step, the approach reported in Ref. [7] requires 980 s in computation with two octa-core Intel processors (E5-2640 v3) and 32 GB RAM, whereas our new approach needs only 4.43 s in the same computation environment, providing performance that is 220 times faster.

Table 2. Values for Si RM Equivalent Circuit Model Parameters for the Case of $D_\lambda = 40$ and 70 pm

V_{Bias} (V)	R_s (Ω)	C_j (fF) $D_\lambda = 40$ and 70 pm	R_1 (kΩ) $D_\lambda = 40$ pm	R_1 (kΩ) $D_\lambda = 70$ pm	C (fF) $D_\lambda = 40$ pm	C (fF) $D_\lambda = 70$ pm	R_2 (kΩ) $D_\lambda = 40$ and 70 pm	L (nH) $D_\lambda = 40$ and 70 pm
0		14.26	0.35	2.07	42.15	7.14	10.00	
−1		10.95	0.75	3.15	19.65	4.70	9.96	
−2	249	9.47	1.77	5.15	8.37	2.87	9.71	114.41
−3		8.55	3.01	7.19	4.92	2.06	9.71	
−4		7.90	4.20	8.99	3.52	1.65	9.71	
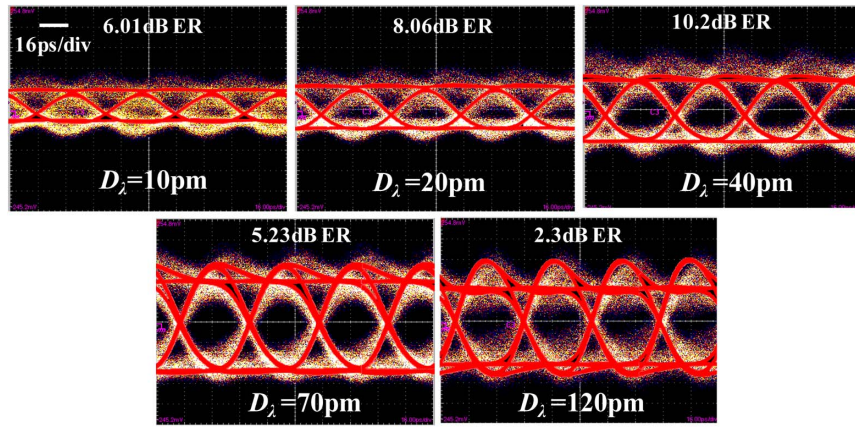
**Fig. 3.** Measured and simulated (red line) 25 Gb/s PRBS31 eye diagrams for different D_λ.

As can be seen in Fig. 3, data with D_λ as 70 pm shows the largest OMA.

3. CO-SIMULATION OF Si RM AND SiGe BiCMOS DRIVER

The real advantage of our model is the ease with which it can be used for co-simulation of electronic circuits and Si RMs. Figure 4(a) shows a schematic diagram for an integrated 25 Gb/s Si photonic transmitter containing a fully differential cascode common-emitter driver and a Si RM. The driver employs the source degeneration technique with R_E to enhance the transmitter bandwidth. This kind of electronic–photonic integrated circuits can be monolithically fabricated with

IHP's photonic BiCMOS technology, which provides high-performance SiGe bipolar transistors having f_T/f_{max} of 220/290-GHz and Si photonic components on the same Si platform [13]. With our RM circuit model, the design optimization of the entire transmitter can be easily carried out.

Figure 4(b) shows the simulated vertical eye opening normalized to the input optical power at different values of I_{tail} and R_L for the case of $D_\lambda = 70$ pm to have the largest OMA. I_{tail} and R_L are key parameters in the driver that determine eye opening, power consumption, and bandwidth. For the simulation, 25 Gb/s $2^{31} - 1$ PRBS NRZ data with a 600 mV swing are supplied to V_{in}^+ and V_{in}^-. Also, the power supply of the driver circuit (V_{cc}) was 4.5 V to have the output data of the driver circuit as $4V_{peak-to-peak}$. Post-layout parasitic
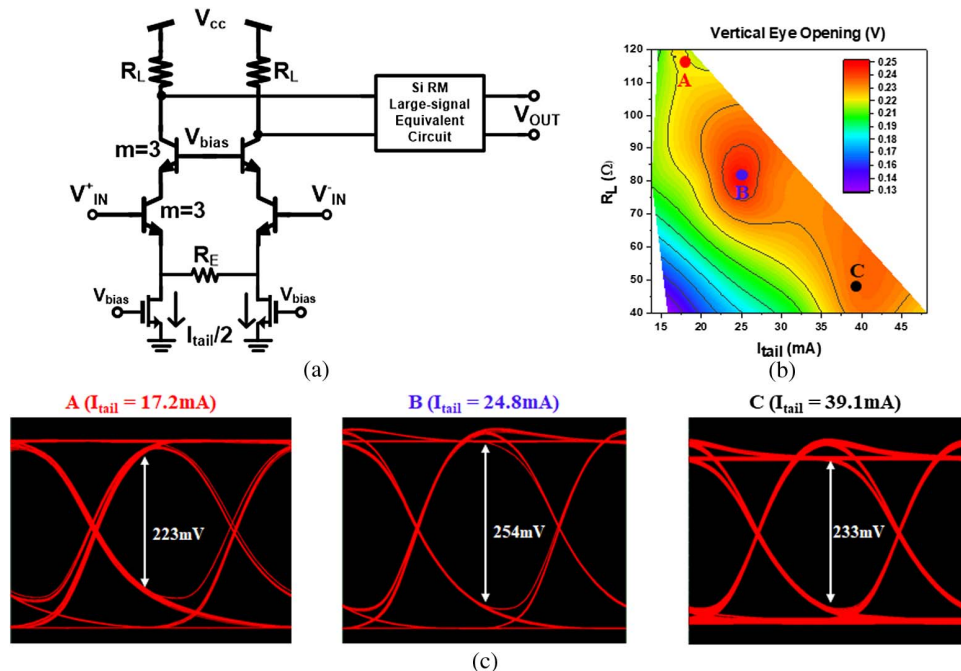
Fig. 4. (a) Schematic diagram for an integrated 25 Gb/s Si photonic transmitter based on Photonic BiCMOS technology; (b) vertical eye opening for various R_L and I_{tail} values; and (c) simulated eye diagrams at different R_L and I_{tail} combinations.

RC values for the driver are included in the simulation since they can significantly influence the driver performance. As can be seen in Fig. 4(b), the vertical eye opening strongly depends on R_L and I_{tail} values. The optimal condition can be determined that provides the largest modulator output eye opening with the smallest I_{tail}, or the smallest power consumption. With a fixed value for R_L, larger I_{tail} generates a larger output voltage swing but runs into the headroom problem if I_{tail} is too large. Figure 4(c) shows simulated eye diagrams at three different conditions, whose I_{tail} and R_L values are represented by Points A, B, and C in Fig. 4(b), having $4V_{peak-to-peak}$ at the driver output. Point A requires a small I_{tail} for peak eye opening but experiences degradation due to a large RC time constant, as shown in the simulated eye diagram. Points B and C show similar eye patterns in terms of rising and falling times but Point C requires a larger I_{tail} due to a smaller R_L, which results in a larger power consumption. Consequently, Point B provides the largest eye opening with the smallest power consumption.

Our RM circuit model can also be used to optimize the ratio of level mismatch (RLM), which is the key performance parameter for a PAM-4 transmitter. RLM is defined as

$$\text{RLM}(\%) = 100 \times \frac{\min(\Delta V_{upper}, \Delta V_{mid}, \Delta V_{lower})}{\text{avg}(\Delta V_{upper}, \Delta V_{mid}, \Delta V_{lower})}, \quad \textbf{(6)}$$
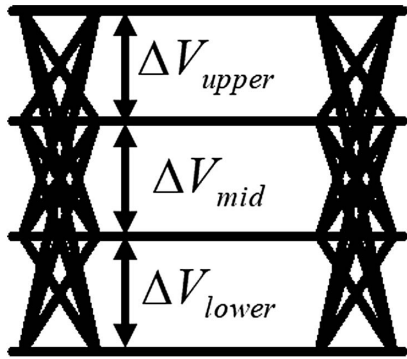
where ΔV_{upper}, ΔV_{mid}, and ΔV_{lower} are defined in Fig. 5. PAM-4 allows a higher data rate transmission without requiring a higher transmitter bandwidth, and it is the standard for many important high-speed I/O applications [14,15]. There is growing interest in PAM-4 based on Si RMs [16–20], but its performance is greatly affected by Si RM nonlinearity, which results in degraded RLM [16–20]. This nonlinearity is due to the Lorentzian shape of the RM resonance as well as the nonlinear dependence of the ring waveguide effective index on the reverse bias [20]. This poses a great challenge to achieve Si PAM-4 transmitters because there is a rather tight requirement on RLM. RLM higher than 94%, for example, is required for IEEE802.3bs and CEI-56G [14,15]. One solution is to apply different driving voltages for ΔV_{upper}, ΔV_{mid}, and ΔV_{lower}, which can compensate for RM nonlinearity [20,21]. To use

Fig. 5. PAM-4 eye diagram and level representation.

Fig. 7. Simulated 25 GBaud PAM-4 eye diagrams at different combination of RLM_{DRV} and D_λ.
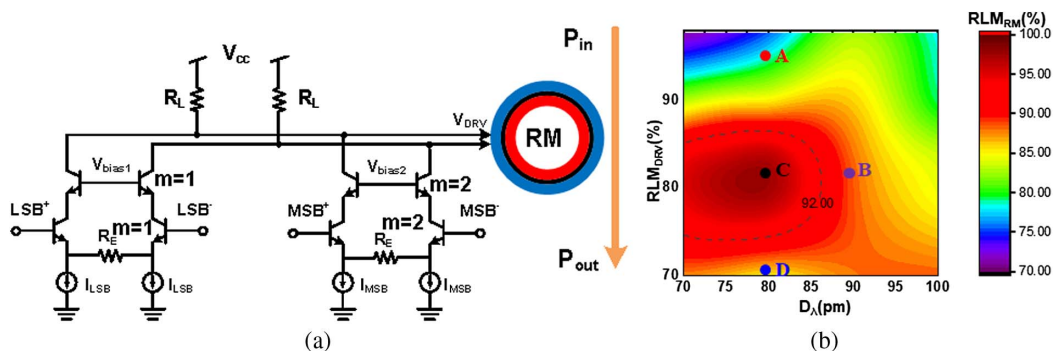

Fig. 6. (a) Schematic diagram of the PAM-4 Si photonic transmitter including driver circuit and the RM and (b) simulated RLM_{RM} values for various combinations of D_λ and RLM_{DRV} values.

Table 3. Operating Conditions and Simulated Results for Different Points in Fig. 6

	RLM_{DRV}	D_λ	RLM_{RM}
Point A	97.8%	80 pm	75.5%
Point B	78.9%	90 pm	88.5%
Point C	78.9%	80 pm	96.9%
Point D	67.2%	80 pm	82.0%

this approach, an accurate co-simulation of a driver circuit and RM is essential.

Figure 6(a) shows a schematic diagram for an integrated 25 GBaud PAM-4 Si photonic transmitter containing a Si RM and a fully differential cascode BiCMOS common-emitter driver with the emitter degeneration based on IHP photonic BiCMOS technology. To determine the optimum PAM-4 modulation condition, SPICE simulation is performed for the integrated transmitter for varying RM D_λ values and different RLM values for the driver output voltages measured between V_{DRV} (RLM_{DRV}). For the simulation, $R_L = 80\ \Omega$ is selected based on the optimization carried out for the above-mentioned NRZ transmitter. Data (25 Gb/s $2^{31} - 1$ PRBS NRZ) is supplied to both inputs of MSB and LSB ports.

The entire transmitter, including the driver and the Si RM, is simulated using the equivalent circuit for Si RM. Figure 6(b) shows the resulting RLM for the Si RM output, or RLM_{RM} for varying driver output voltage RLM, or RLM_{DRV}, and detuning. Different RLM_{DRV} values are achieved by changing I_{LSB} and I_{MSB}, while their sum is kept the same and V_{DRV} has a $4V_{peak-to-peak}$ swing. As can be seen in the figure, RLM_{RM} over 94% can be achieved when D_λ is about 80 pm and the RLM_{DRV} is between about 75% and 85%. Figure 7 shows the simulated eye diagrams for the driver and RM outputs in different conditions represented by Points A, B, C, and D in Fig. 6(b), and such conditions and results are described in Table 3. At Point A, RLM_{DRV} is almost 100% but RLM_{RM} is significantly degraded due to Si RM nonlinearity. The RM nonlinearity is such that the middle eye opening is the largest. Consequently, by distorting driver output or making the middle eye smaller, RLM_{RM} can be improved, as shown by the Points B and C eye diagrams. Too much driver output distortion causes RLM_{RM} degradation, as shown by the Point D eye diagram. With the optimum distortion of the driver output, we can carefully choose the detuning for the maximum RLM_{RM}, as Point C shows an almost 97% RLM value.

4. CONCLUSION

We demonstrate a new large-signal SPICE circuit model for a depletion-type Si RM. The model is accurate, easy to use, and allows a significantly reduced simulation time compared to the previously reported approach. The accuracy of the model is confirmed with measured 25 Gb/s NRZ modulation results at different detuning values. Furthermore, the model allows easy co-simulation with electronic driver circuits. We demonstrate the design optimization based on such co-simulation for Si NRZ and PAM-4 transmitters containing SiGe BiCMOS drivers and Si RMs.

REFERENCES

1. G. Li, A. V. Krishnamoorthy, I. Shubin, J. Yao, Y. Luo, H. Thacker, X. Zheng, K. Raj, and J. E. Cunningham, "Ring resonator modulators in silicon for interchip photonic links," IEEE J. Sel. Top. Quantum Electron. **19**, 95–113 (2013).
2. B. M. M. Milosevic, S. Stankovic, S. Reynolds, T. D. Bucio, K. Li, D. J. Thomson, F. Gardes, and G. T. Reed, "The emergence of silicon photonics as a flexible technology platform," Proc. IEEE **106**, 2101–2116 (2018).
3. J. Sun, R. Kumar, M. Sakib, J. B. Driscoll, H. Jayatilleka, and H. Rong, "A 128 Gb/s PAM-4 silicon microring modulator with integrated thermo-optic resonance tuning," J. Lightwave Technol. **37**, 110–115 (2019).
4. Y. Kim, Y. Jo, M. Kim, B.-M. Yu, C. Mai, S. Lischke, L. Zimmermann, and W.-Y. Choi, "Parametric optimization of depletion-type Si microring modulator performances," Jpn. J. Appl. Phys. **58**, 062006 (2019).
5. A. H. Atabaki, S. Moazeni, F. Pavanello, H. Gevorgyan, J. Notaros, L. Alloatti, M. T. Wade, C. Sun, S. A. Kruger, H. Meng, K. Al Qubaisi, I. Wang, B. Zhang, A. Khilo, C. V. Baiocco, M. A. Popović, V. M. Stojanović, and R. J. Ram, "Integrating photonics with silicon nanoelectronics for the next generation of systems on a chip," Nature **556**, 349–354 (2018).
6. R. Dube-Demers, J. St-Yves, A. Bois, Q. Zhong, M. Caverley, Y. Wang, L. Chrostowski, S. LaRochelle, D. V. Plant, and W. Shi, "Analytical modeling of silicon microring and microdisk modulators with electrical and optical dynamics," J. Lightwave Technol. **33**, 4240–4252 (2015).
7. J. Rhim, Y. Ban, B.-M. Yu, J.-M. Lee, and W.-Y. Choi, "Verilog-A behavioral model for resonance-modulated silicon micro-ring modulator," Opt. Express **23**, 8762–8772 (2015).
8. M. Shin, Y. Ban, B. M. Yu, M. H. Kim, J. Rhim, L. Zimmermann, and W. Y. Choi, "A linear equivalent circuit model for depletion-type silicon microring modulators," IEEE Trans. Electron Devices **64**, 1140–1145 (2017).
9. M. Kim, M. Shin, M.-H. Kim, B.-M. Yu, C. Mai, S. Lischke, L. Zimmermann, and W.-Y. Choi, "A large-signal equivalent circuit for depletion-type silicon ring modulators," in *Optical Fiber Communication Conference* (OSA, 2018), paper Th2A.13.
10. B. E. Little, S. T. Chu, H. A. Haus, J. Foresi, and J.-P. Laine, "Microring resonator channel dropping filters," J. Lightwave Technol. **15**, 998–1005 (1997).
11. Y. Ban, J. M. Lee, B. M. Yu, S. H. Cho, and W. Y. Choi, "Small-signal frequency responses for Si micro-ring modulators," in *IEEE Optical Interconnects Conference (OI'14)* (2014), pp. 47–48.
12. Optilab PR-23-M, 23 GHz Linear Photoreceiver Module, 2018, https://www.oequest.com/getDatasheet/id/10580-10580.pdf.
13. D. Knoll, S. Lischke, A. Awny, and L. Zimmermann, "SiGe BiCMOS for optoelectronics," ECS Trans. **75**, 121–139 (2016).
14. IEEE P802.3 bs 200 Gb/s and 400 Gb/s Ethernet Task Force. http://www.ieee802.org/3/bs/.
15. OIF CEI-56G Application Note. https://www.oiforum.com/.
16. A. Roshan-Zamir, B. Wang, S. Telaprolu, K. Yu, C. Li, M. A. Seyedi, M. Fiorentino, R. Beausoleil, and S. Palermo, "A 40 Gb/s PAM-4 silicon microring resonator modulator transmitter in 65 nm CMOS," in *IEEE Optical Interconnects Conference (OI)* (2016), pp. 8–9.
17. R. Li, D. Patel, A. Samani, E. El-Fiky, Z. Xing, M. Morsy-Osman, and D. V. Plant, "Silicon photonic ring-assisted MZI for 50 Gb/s DAC-less and DSP-free PAM-4 transmission," IEEE Photon. Technol. Lett. **29**, 1046–1049 (2017).
18. R. Li, D. Patel, E. El-Fiky, A. Samani, Z. Xing, M. Morsy-Osman, and D. V. Plant, "High-speed low-chirp PAM-4 transmission based on

push-pull silicon photonic microring modulators," Opt. Express **25**, 13222–13229 (2017).

19. S. Moazeni, S. Lin, M. Wade, L. Alloatti, R. J. Ram, M. Popovic, and V. Stojanovic, "A 40-Gb/s PAM-4 transmitter based on a ring-resonator optical DAC in 45-nm SOI CMOS," IEEE J. Solid-State Circuits **52**, 3503–3516 (2017).

20. H. Li, G. Balamurugan, M. Sakib, J. Sun, J. Driscoll, R. Kumar, H. Jayatilleka, H. Rong, J. Jaussi, and B. Casper, "A 112 Gb/s PAM-4 transmitter with silicon photonics microring modulator and CMOS driver," in *Optical Fiber Communication Conference* (OSA, 2019), paper Th4A.4.

21. T. Kishi, M. Nagatani, S. Kanazawa, W. Kobayashi, H. Yamazaki, M. Ida, K. Kurishima, M. Nogawa, S. Kimura, and H. Nosaka, "56 Gb/s optical transmission performance of an InP HBT PAM-4 driver compensating for nonlinearity of extinction curve of EAM," J. Lightwave Technol. **35**, 75–81 (2017).